Combined In Situ EDXRD/EXAFS Investigation of the Crystal Growth of $[Co(C_6H_{18}N_4)][Sb_2S_4]$ under Solvothermal Conditions: Two Different Reaction Pathways Leading to the Same Product

Ragnar Kiebach, Nicole Pienack, Marie-Eve Ordolff, Felix Studt, and Wolfgang Bensch*

Institute of Inorganic Chemistry, University of Kiel, Olshausenstrasse 40-60, 24098 Kiel, Germany

Received August 10, 2005. Revised Manuscript Received November 23, 2005

The crystal growth and kinetics of the formation of $[Co(C_6H_{18}N_4)][Sb_2S_4]$ were investigated under solvothermal conditions with combined in situ EDXRD (energy dispersive X-ray diffraction) and in situ EXAFS (extended X-ray absorption fine structure) at different temperatures. In the overwhelming number of reactions all product reflections occur simultaneously in the EDXRD spectra. A detailed analysis of the extent of reaction α vs time clearly shows that the mechanism changes during the reaction. Such a change occurs at different temperatures after different reaction times. At the early stages the reactions are controlled by diffusion, and later the reaction exponents *m* suggest a more complex behavior. At the end of the formation of $[Co(C_6H_{18}N_4)][Sb_2S_4]$ a second phase is formed which does not contain Co. The results of the in situ experiments suggest that $[Co(C_6H_{18}N_4)][Sb_2S_4]$ is not only a metastable phase but rather that the second product crystallizes because the Co^{2+} concentration in solution is too low for further formation of $[Co(C_6H_{18}N_4)][Sb_2S_4]$. In the minor cases of the solvothermal reaction a very different growth was observed. At the beginning only one intense reflection occurs in the spectra and after a distinct time all other reflections start to grow simultaneously. This strange behavior indicates that disordered layers are formed at the beginning which start to arrange at later stages, yielding the three-dimensional long-range order. The in situ EXAFS experiments performed at the Sb K-edge demonstrate that, independent of the reaction time, the Sb/S ratio, and the amine applied, only the two species SbS_3 and SbS_4 are present in solution.

Introduction

Cobalt-containing frameworks are of great interest in catalysis and a lot of research has been done in this field. Important catalysts are cobalt-containing acidic zeolites for hydrodesulfurization.[1] Thioantimonates(III) with zeotype structures are also possible candidates for catalytic applications. In recent years a large number of microporous thioantimonates(III)[2−5] have been synthesized. A good example to demonstrate the structural relationship between thioantimonates(III) and zeolites is the three-dimensional cobalt-containing compound $[Co(en)_3][Sb_{12}S_{19}]$[6] with channels being comparable with those in ZSM-5. The combination of the useful properties of zeolites with manifold properties of thioantimonates(III) like tunable optical band gaps,[7] superconductivity,[8] or photoconductivity[9] should lead to a new class of compounds with designed physical properties. Recently, we published the synthesis and structure of the layered compound $[Co(tren)][Sb_2S_4]$[10] (tren = tris(2-aminoethyl)amine) in which Co^{2+} is part of the thioantimonate(III) network (Figure 1). Such a combination makes the material of interest for further applications and investigations are in progress. Microporous materials are synthesized under solvothermal conditions with organic molecules acting as structure directors. The final crystalline products often show a low density and can be regarded as kinetic controlled products.

Despite the importance of the solvothermal method for the synthesis of new materials such as catalysts, ion exchangers, and porous materials, the reaction mechanisms leading to the crystalline products are not well-understood. Compared to the enormous number of experiments performed under solvothermal conditions, experiments for understanding the mechanisms, the kinetics of solvothermal syntheses, and exploration of the influence of reaction parameters such as temperature, pH value, and volume are quite rare. In the past decade the number of publications[11−16] presenting results of in situ energy-dispersive X-ray diffraction (EDXRD) studies

* To whom correspondence should be addressed. Tel: +49 431 880-2406. Fax: +49 431 880-1520. E-mail: wbensch@ac.uni-kiel.de.

(1) Korányi, T. I.; Pham, N. G.; Jentys, A.; Vinek, H. *Stud. Surf. Sci. Catal.* **1997**, *106*, 509.
(2) Stähler, R.; Näther, C.; Bensch, W. *J. Solid State Chem.* **2003**, *174*, 264.
(3) Wang, X.; Liebau, F. *J. Solid State Chem.* **1994**, *111*, 385.
(4) Spetzler, V.; Kiebach, R.; Näther, C.; Bensch, W. *Z. Anorg. Allg. Chem.* **2004**, *630*, 2398.
(5) Kiebach, R.; Näther, C.; Bensch, W. *Z. Naturforsch.* **2004**, *59b*, 1314.
(6) Vaqueiro, P.; Chippindale, A. M.; Powell, A. V. *Inorg. Chem.* **2004**, *43*, 7963.
(7) Schaefer, M.; Stähler, R.; Kiebach, W.-R.; Näther, C.; Bensch, W. *Z. Anorg. Allg. Chem.* **2004**, *630*, 1816.
(8) Lee, C.-S.; Safa-Sefat, A.; Greedan, J. E.; Kleinke, H. *Chem. Mater.* **2003**, *15*, 780.
(9) Starrost, F.; Krasovskii, E. E.; Schattke, W.; Simon, U.; Wang, X.; Liebau, F. *Phys. Rev. Lett.* **1998**, *80*, 3316.
(10) Stähler, R.; Bensch, W. *Eur. J. Inorg. Chem.* **2001**, 3073.
(11) Kiebach, R.; Schaefer, M.; Porsch, F.; Bensch, W. *Z. Anorg. Allg. Chem.* **2005**, *631*, 369.
(12) Engelke, L.; Schaefer, M.; Porsch, F.; Bensch, W. *Eur. J. Inorg. Chem.* **2003**, 506.

10.1021/cm051788t CCC: $33.50
Published on Web 02/08/2006

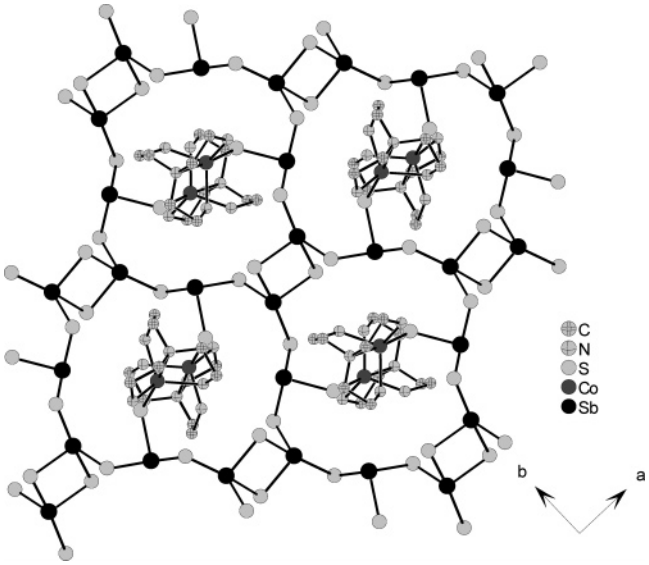

Figure 1. Crystal structure of [Co(tren)][Sb_2S_4] viewed along the *c*-axis.

of solvothermal reaction has grown constantly, but the number of reports is still low. EDXRD is a powerful method to investigate the influence of different parameters onto the formation of crystalline products. Crystalline precursors and/or intermediates are detected without quenching the reaction and without workup of the product. But with EDXRD only crystalline phases can be detected, and amorphous phases and very small precursors in the liquid phase cannot be observed so this part of the reaction is still a kind of "black box". Information from amorphous phases or molecules in solution can be acquired with extended X-ray absorption fine structure (EXAFS) experiments because data about the local structure and the local atomic coordination are collected.[17−19] The combination of these two complementary methods yields a much better understanding of the mechanisms occurring during chemical reactions.[20−24] Here we report the EDXRD/EXAFS studies of the system Co/Sb/S/tren, and the kinetic results of the crystal growth of [Co(tren)][Sb_2S_4] are presented.

Experimental Section

The compound [Co($C_6H_{18}N_4$)][Sb_2S_4] is obtained by reacting elemental Co (29 mg, 0.5 mmol, Fluka, purum p.a.), Sb (61 mg, 0.5 mmol, Fluka, purum p.a.), and S (48 mg, 1.5 mmol, Fluka, purum p.a.) in 2 mL of an aqueous tren (purum, Fluka) solution (50%) as solvent. The temperature range for the experiments varied between 105 and 130 °C. Note that above 130 °C only [Co(tren)-Sb_4S_7] is formed, below 105 °C no product growth could be observed within 5 h, and under static conditions the reaction required several days for completion. The reaction was studied at 105, 110, 115, 120, 125, and 130 °C under isothermal conditions. Additional experiments with $CoCl_2 \cdot 6H_2O$ (119 mg, 0.5 mmol, Fluka) were carried out at 120 °C.

Synchrotron Radiation Source for EDXRD Measurements. HASYLAB Beamline F3 receives white synchrotron radiation from a bending magnet with a critical energy of 16 keV and gives a positron beam energy of 4.5 GeV. An energy range from 13.5 to 65 keV can be observed with a maximum at about 20 keV. The diffracted beam is monitored by a nitrogen-cooled solid-state germanium detector. The detector angle of approximately 1.90° allowed the detection of Bragg reflections with *d* spacing from 2.9 to 13.8 Å. The energy resolution $\Delta d/d$ was about 10^{-2} above 26 keV. The beam was collimated to 0.2 mm, giving the best results. More experimental details are found in refs 12 and 13. The in situ investigations were conducted with autoclaves containing glass liners with an internal diameter of 10 mm and a volume of 10 mL.

Synchrotron Radiation Source for EXAFS Measurements. The experiments were performed in transmission at the Sb K edge (30491 eV) at beamline X1 (HASYLAB). A Si(311) double crystal was used as monochromator and the measurement time was about 260 s for each scan. The storage ring operated with injection currents of 140 mA at 4.4 GeV. The stirring of the reaction mixture was interrupted every second spectrum for data acquisition of Sb in solution without influence of the solid phase.

Details of data reduction procedures for energy dispersive X-ray absorption spectra can be found in the literature.[25,26] The data analysis was done with WinXAS 3.0 following recommended procedures.[27] Pre-edge background subtraction and normalization were carried out fitting linear polynomials to the pre-edge and the post-edge region of the spectra, respectively. A smooth atomic background was obtained with a cubic spline refinement procedure. Fitting range in *k* space, number of splines, and *k* weighting were optimized to afford a rigid background curve at low *k* and minimization of low *R* peaks in the Fourier transformed signal. The radial distribution function $FT(\chi(k))$ was obtained by Fourier-transforming the k^3 weighted experimental extended fine structure (EXAFS) $\chi(k)$, multiplied by a Bessel window, into *R* space.

Calculation of theoretical EXAFS spectra and refinement of experimental data were carried out using theoretical backscattering phases and amplitudes obtained from the ab initio multiple-scattering code FEFF 7.[28] Parameters obtained with a least-squares fit of the standard EXAFS formula are S_0^2, the passive electron reduction factor, R_j, the interatomic distance, the Debye−Waller factor σ_j^2, and the coordination number CN.

EXAFS refinements were carried out in *R* space to the magnitude and imaginary parts of a Fourier-transformed k^3 weighted experimental $\chi(k)$. Further details on the EXAFS refinement procedure employed can be found in ref 29.

(13) Engelke, L.; Schaefer, M.; Schur, M.; Bensch, W. *Chem. Mater.* **2001**, *13*, 1383.
(14) Francis, R. J.; Price, J. S.; Evans, J. S. O.; O'Brien, S.; O'Hare, D. *Chem. Mater.* **1996**, *8*, 2102.
(15) Bray, H. J.; Redfern, S. A. T. *Phys. Chem. Miner.* **1999**, 591.
(16) Christensen, A. N.; Bareges, A.; Nielsen, R. N.; Hazell, R. G.; Norby, P.; Hanson, J. C. *J. Chem. Soc., Dalton Trans.* **2001**, 1611.
(17) Penner-Hahn, J. E. *Coord. Chem. Rev.* **1999**, *190−192*, 1101.
(18) Burattini, E.; Dalba, G.; Fornasini, P. *Il Nuovo Cimento* **1986**, *7*, 293.
(19) Cervinka, L.; Smotlacha, O.; Bererová, J.; Tichy, L. *Non.-Cryst. Solids* **1991**, *137−138*, 123.
(20) Sankar, G.; Rey, F.; Thomas, J. M.; Greaves, G. N.; Corma, A.; Dobson, B. R. *J. Chem. Soc., Chem. Commun.* **1994**, 2279.
(21) Thomas, J. M. *Angew. Chem.* **1999**, *111*, 3800.
(22) Rey, F.; Sankar, G.; Thomas, J. M.; Barrett, P. A.; Lewis, D. W.; Catlow, C. R. A.; Clark, S. M.; Greave, G. N. *Chem. Mater.* **1995**, *7*, 1435.
(23) Sankar, G.; Wright, P. A.; Natarajan, S.; Thomas, J. M.; Greaves, G. N.; Dent, A. J.; Dobson, B. R.; Ramsdale, C. A.; Jones, R. H. *J. Phys. Chem.* **1993**, *97*, 9550.
(24) Cora, F.; Sankar, G.; Catlow, C. R. A.; Thomas, J. M. *Chem. Commun.* **2002**, 734.
(25) Ressler, T. *J. Phys. IV* **1997**, *7*, C2−C269.
(26) Ressler, T.; Hagelstein, M.; Hatje, U.; Metz, W. *J. Phys. Chem. B* **1997**, *101*, 6680.
(27) Koningsberger, D. C.; Prins, R. *X-Ray Absorption Spectroscopy, Chemical Analysis*, Wiley: NewYork, 1988.
(28) Rehr, J. J.; Booth, C. H.; Bridges, F.; Zabinsky, S. I. *Phys. Rev. Lett.* **1992**, *69*, 3397.
(29) Ressler, T.; Timpe, O.; Neisius, T.; Find, J.; Mestl, G.; Dieterle; M. Schlögl, R. *J. Catal.* **2000**, *191*, 75.

The FT spectra showed only one shell and the fitting must be done with care. The parameters S_0^2, CN, R_j, and σ^2 are correlated and some assumptions must be made to get reliable results. The factor S_0^2 depends on the free path lengths which in turn scales with the temperature. The spectra were recorded at 130 °C and a fixed value of 1.05 is reasonable. For Sb-containing solutions different values for σ^2 were reported which were used as the upper and lower limit during the refinements; i.e., σ^2 was freely refined within this range. The resulting magnitudes for σ^2 (Table 3) are in excellent agreement with those reported in previous papers.[30,31] The interatomic distance R_j depends on E_0 (zero point of the energy scale) which was fixed to 10 eV in accordance with literature data. Refinement of E_0 with starting values far from 10 always yielded a value very near to 10. The spectra were then refined either with the SbS_3 or the SbS_4 unit with a freely varying CN. In both cases the value for CN was 3.6, giving lower reliability factors than using the same units with fixed coordination numbers. In the next step the spectra were refined with fixed coordination numbers but with a variable ratio of both species. The lowest reliability factor was obtained for a 1:1 mixture of SbS_3 and SbS_4.

Reference measurements were done with a pressed pellet obtained by mixing about 100 mg [Co(tren)][Sb_2S_4] with boron nitride (ratio 1:3). The in situ experiments were performed in the above-mentioned cell under autogenous pressure either under dynamic (with stirring) or static (without stirring) conditions. At the end of the reaction the solid product was used as the reference phase.

For Sb references in the liquid phase 3.04 g (25 mmol) of Sb and 2.4 g (75 mmol) of S were dissolved in 100 mL of a 50% aqueous diethylenediamine solution and heated under reflux for 2 h. The resulting parent solution (A1) was diluted with 50 vol % water (A2). This solution was again diluted with 50 vol % water, yielding A3, and this procedure was continued until solution A15 was obtained, which contained 0.003% of solution A1.

Density Functional Theory Calculations. Spin-restricted DFT calculations using Becke's three-parameter hybrid functional with the correlation functional of Lee, Yang, and Parr (B3LYP)[32−34] were performed for the singlet ground state of SbS_3^{3-} and SbS_4^{5-}. The LANL2DZ basis set was used for the calculations. It applies Dunning/Huzinaga full double-ζ (D95) basis functions[35] on the first row and Los Alamos effective core potentials plus DZ functions on all other atoms.[36,37] All computational procedures were used as they are implemented in the Gaussian 98 package.[38]

(30) Frederick, J.; Mosselmans, W.; Helz, G. R.; Pattrick, R. A. D.; Charnock, J. M.; Vaughan, D. J. *Appl. Geochem.* **2000**, *15*, 879.
(31) Oelkers, E. H.; Sherman, D. M.; Ragnarsdottir, K. M.; Collins, C. *Chem. Geol.* **1998**, *151*, 21.
(32) Becke, A. D. *Phys. Rev. A* **1988**, *38*, 3098.
(33) Becke, A. D. *J. Chem. Phys.* **1993**, *98*, 1372.
(34) Becke, A. D. *J. Chem. Phys.* **1993**, *98*, 5648.
(35) Dunning, T. H., Jr.; Hay, P. J. In *Modern Theoretical Chemistry*; Schaefer, H. F., III, Ed.; Plenum: New York, 1976.
(36) Hay, P. J.; Wadt, W. R. *J. Chem. Phys.* **1985**, *82*, 270.
(37) Wadt, W. R.; Hay, P. J. *J. Chem. Phys.* **1985**, *82*, 284.
(38) Frisch, M. J.; Trucks, G. W.; Schlegel, H. B.; Scuseria, G. E.; Robb, M. A.; Cheeseman, J. R.; Zakrzewski, V. G.; Montgomery, J. A., Jr.; Stratmann, R. E.; Burant, J. C.; Dapprich, S.; Millam, J. M.; Daniels, A. D.; Kudin, K. N.; Strain, M. C.; Farkas, O.; Tomasi, J.; Barone, V.; Cossi, M.; Cammi, R.; Mennucci, B.; Pomelli, C.; Adamo, C.; Clifford, S.; Ochterski, J.; Petersson, G. A.; Ayala, P. Y.; Cui, Q.; Morokuma, K.; Salvador, P.; Dannenberg, J. J.; Malick, D. K.; Rabuck, A. D.; Raghavachari, K.; Foresman, J. B.; Cioslowski, J.; Ortiz, J V.; Baboul, A. G.; Stefanov, B. B.; Liu, G.; Liashenko, A.; Piskorz, P.; Komaromi, I.; Gomperts, R.; Martin, R. L.; Fox, D. J.; Keith, T.; Al-Laham, M. A.; Peng, C. Y.; Nanayakkara, A.; Challacombe, M.; Gill, P. M. W.; Johnson, B.; Chen, W.; Wong, M. W.; Andres, J. L.; Gonzalez, C.: Head-Gordon, M.; Replogle, E. S.; Pople. J. A. *Gaussian98*, Rev. A.11; Gaussian, Inc.: Pittsburgh, PA, 2001.

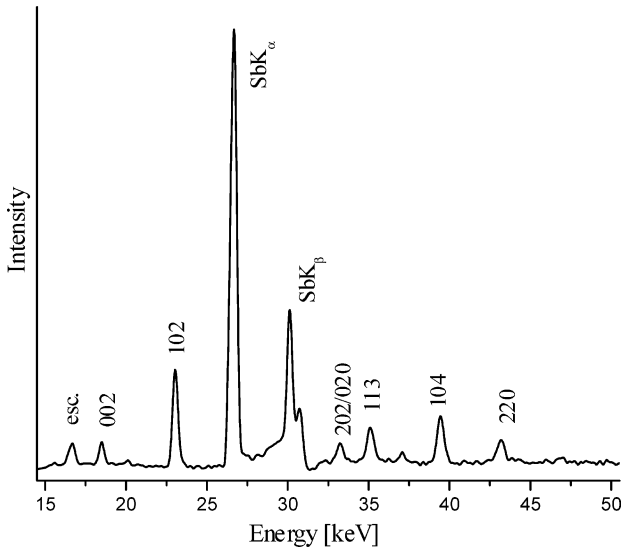

Figure 2. Energy dispersive diffraction pattern of [Co(tren)][Sb_2S_4]. The indices of the reflections and the Sb fluorescence are marked.

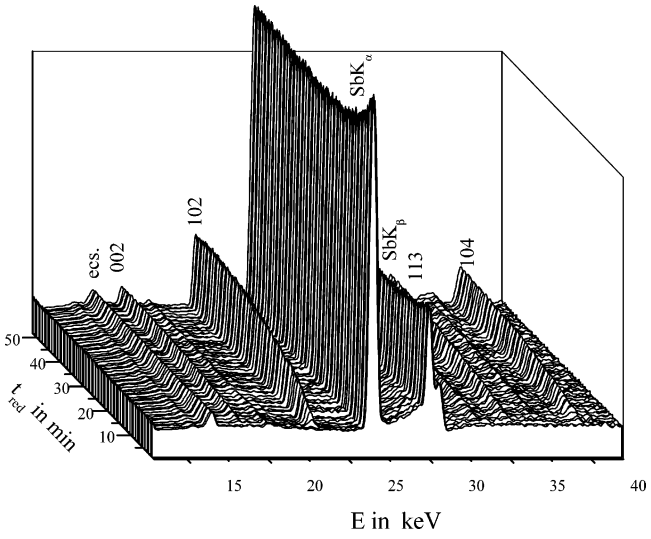

Figure 3. Time-resolved powder pattern recorded at 120 °C. The indices of the most intense lines of the product phase and the Sb Kα fluorescence line are marked.

Results and Discussion

EDXRD. In the spectra several reflections of the product and the Sb resonance are monitored simultaneously (Figure 2). A typical sequence of time-resolved spectra is shown in Figure 3. After an induction time, t_{ind}, which strongly depends on the reaction temperature, product peaks starts to grow. Note that the Sb resonance at 26.6 and 31.1 keV as well as an escape peak at 16.5 keV are immediately visible in the spectra. The (102) reflection with the highest intensity corresponds to the layers of the compound. A quantitative analysis of the growth rates shows an identical behavior for different reflections and confirms an isotropic crystallite growth (see also below). In the spectra no hints are seen for the occurrence of crystalline precursors or intermediates. Compared to t_{ind} the half-life time $t_{0.5}$ of crystallization is short and is about 15% of the time necessary to complete the reaction (Table 1). The first step of the kinetic analysis is the integration of one or several product reflections using a Gaussian function and measuring the corresponding areas.

Table 1. Kinetic Data Obtained by the Analysis with Sharp-Hanckock Plots

T in °C	induction time[a] in min	reaction time[b] in min	half-life time[c] in min	m	$k[s^{-1}] \times 10^{-4}$
105 α < 0.71	204	200	18	0.57	5.20
α > 0.71				0.85	4.29
110 α < 0.77	113	133	17	0.66	5.45
α > 0.77				1.29	4.43
115 α < 0.75	101	62	15	0.59	6.39
α > 0.75				1.23	4.64
120 α < 0.68	83	47	9	0.70	8.74
α > 0.68				1.65	8.28
125 α < 0.53	66	45	9	0.67	10.13
α > 0.53				0.98	11.18
130 α < 0.67	56	38	7	0.55	10.74
α > 0.67				1.41	10.81

[a] Induction time: time between reaction start and occurrence of first product peaks. [b] Reaction time: time between first occurrence of product peaks and end of reaction (α = 1). [c] Half-life time: time between first occurrence of product peaks and α = 0.5.

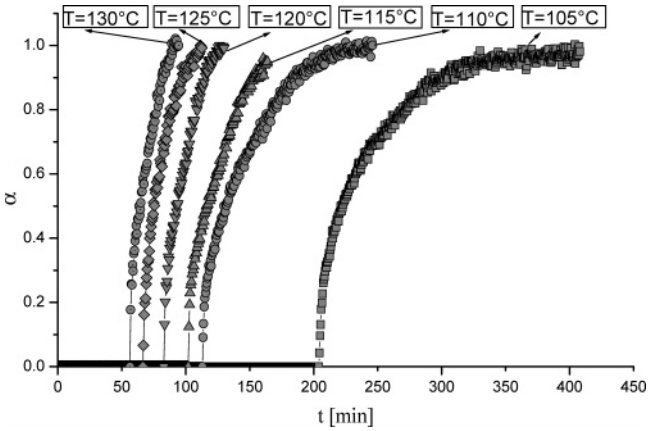

Figure 4. Extent of reaction α versus time for the (102) reflection at different reaction times.

These are then converted to the extent of reaction α using the relation $\alpha(t) = I_n(t)/I_n(t\infty)$, with $I_n(t)$ being the intensity of the reflection at time t and $I_n(t\infty)$ is the intensity of this reflection at the end of the reaction ($t = \infty$). In the present analysis the previously integrated intensities at time t were divided by the intensity of the Sb Kα resonance peak at the same time t to get the normalized intensity relative to the beam intensity; i.e., the data are very accurate due to the correction for fluctuation of primary beam intensity.

The plot of α vs reaction time t (Figure 4, Table 1) shows a strong temperature dependence of t_{ind}. At 130 °C the value for t_{ind} is 56 min and increases by a factor of 4 at 105 °C (t_{ind} = 204 min). It is remarkable that the data are reproducible on a very high level despite the long induction period at 105 °C, and according to experimental results the variation of t_{ind} is less than 5 min (<2.5%) at 105 °C.

Kinetic Analysis. Kinetic analyses are performed by fitting the experimental data to a theoretical expression relating the extent of reaction α vs time. Several kinetic expressions applied to solid-state kinetics are reported, and the general shape of their curves is well-documented. A detailed description of the procedure for the evaluation of the data was presented for instance in ref 12.

The kinetic evaluation was performed after subtraction of t_{ind} from time t and the reduced reaction time (t_{red}) is obtained. The kinetic data for different reaction temperatures are summarized in Table 1. When $\ln[-\ln(1-\alpha)]$ is plotted vs $\ln(t)$ (the so-called Sharp-Hancock plot, abbreviated SH) a straight line is obtained for that part of the reaction which follows the same mechanism.[39−41] A change of the mechanism results in a change of the slope of the curve. From the slope of the linear part of the curve the reaction exponent m can be evaluated (often called the Avrami exponent) and the intercept with the y axis gives the rate constant k [s^{-1}]. The exponent m is then related to the type of nucleation and growth process taking place, including the morphology of the reaction product, i.e., whether the crystals are fibers, needles, plates, sheets, spheres, or polygons. The exponent m also includes the type of nucleation, i.e., whether the nuclei all develop at once or continuous nucleation with a constant rate occurs.[42,43]

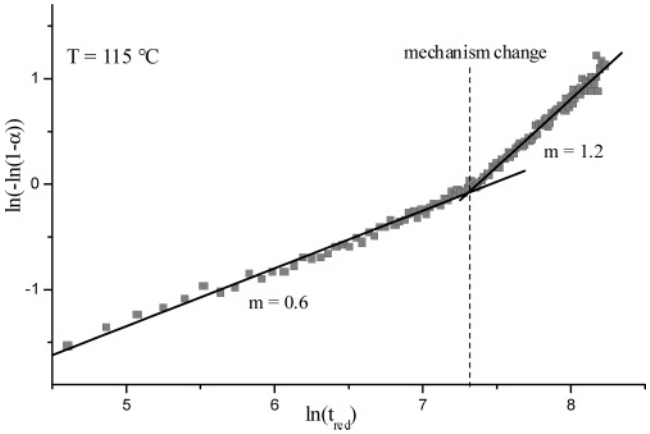

Figure 5. Sharp-Hanckock plot for the data at T = 115 °C.

Table 2. Rate Equations for Solid-State Reactions Reported in the Literature

growth model	*rate equation* $f(\alpha) = kt$	*m*
	Diffusion-Controlled	
$D_1(\alpha)$	$\alpha^2 = 0.25\ (t/t_{0.5})$	0.62
$D_2(\alpha)$	$(1-\alpha)\ln(1-\alpha)+\alpha = 0.1534\ (t/t_{0.5})$	0.57
$D_3(\alpha)$ [Jander]	$[1-(1-\alpha)^{1/3}]^2 = 0.0425\ (t/t_{0.5})$	0.54
$D_4(\alpha)$ [Ginstling-Brounshtein]	$1-2\alpha/3-(1-\alpha)^{2/3} = 0.0367\ (t/t_{0.5})$	0.57
	Phase-Boundary-Controlled	
$R_2(\alpha)$	$1-(1-\alpha)^{1/2} = 0.2929\ (t/t_{0.5})$	1.11
$R_3(\alpha)$	$1-(1-\alpha)^{1/3} = 0.2063\ (t/t_{0.5})$	1.07
	First Order	
F1(α)	$[-\ln(1-\alpha)] = 0.6931\ (t/t_{0.5})$	1.00
	Nucleation [Avrami-Erovéef]	
A2(α)	$[-\ln(1-\alpha)]^{1/2} = 0.8326\ (t/t_{0.5})$	2.00
A3(α)	$[-\ln(1-\alpha)]^{1/3} = 0.885\ (t/t_{0.5})$	3.00

The SH plot for data obtained at T = 115 °C (Figure 5) clearly shows that the growth can be divided into two different parts. Up to $\alpha \approx 0.77$ the reaction exponent m has a value of 0.59 corresponding to a diffusion controlled growth mechanism (Table 2), and in the second part ($\alpha > 0.77$) m increases to about 1.23. For reactions at $T \leq 110$ °C the experimental points are on a straight line nearly over

(39) Hancock, J. D.; Sharp, J. H. *J. Am. Ceram. Soc*. **1972**, *55*, 74.
(40) Sharp, J. H.; Brindley, G. W.; Narahari Achar, B. N. *J. Am. Ceram. Soc*. **1966**, 379.
(41) Mohamed, B. M.; Sharp, J. H. *J. Mater. Sci*. **1997**, 1595.
(42) Brown, P. W.; Pommersheim, J.; Frohnsdorff, G. *Cem. Concr. Res.* **1985**, *15*, 35.
(43) Thomas, J. J.; Jennings, H. M. *Chem. Mater*. **1999**, *11*, 1907.

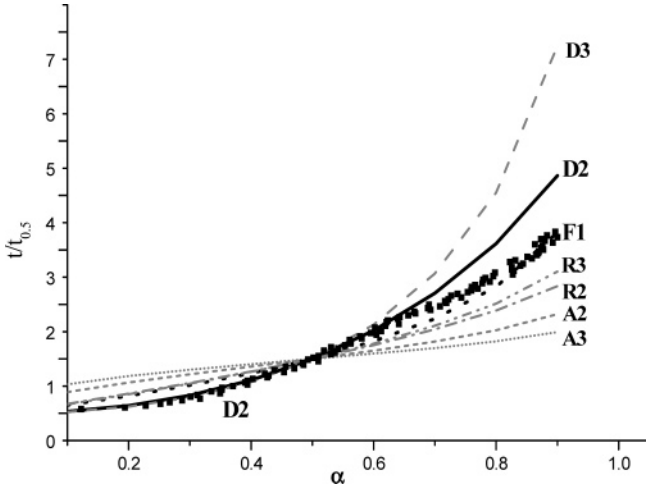

Figure 6. Comparison of experimental $t/t_{0.5}$ data as a function of α (black squares) with different theoretical models for $T = 115$ °C. The letters with the numbers are abbreviations of the different models listed in Table 2.

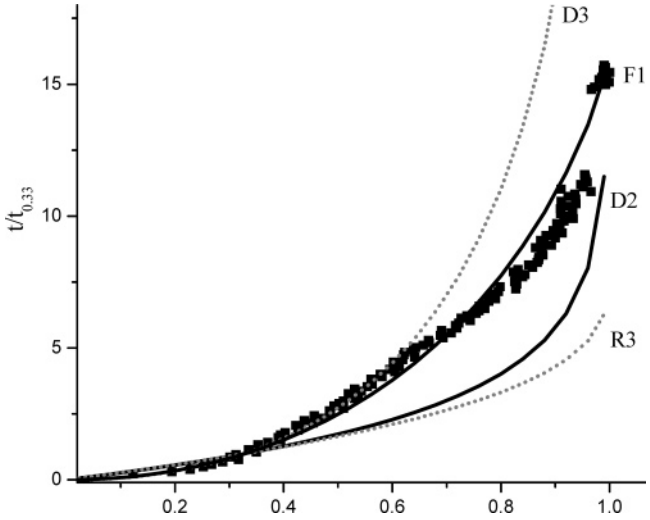

Figure 7. Comparison of experimental $t/t_{0.3}$ data as a function of α (black squares) with different theoretical models for $T = 115$ °C. The letters with the numbers are abbreviations of the different models listed in Table 2.

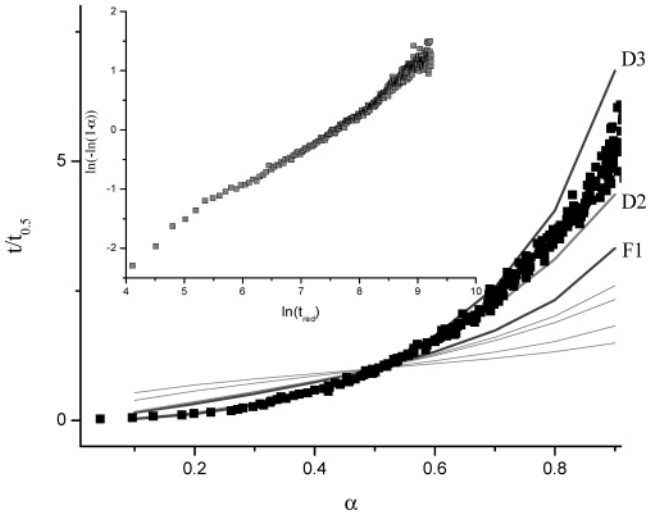

Figure 8. Comparison of experimental $t/t_{0.5}$ data as a function of α (black squares) with different theoretical models for $T = 105$ °C. The letters with the numbers are abbreviations of the different models listed in Table 2. Inset: Sharp-Hanckock plot for the data at $T = 105$ °C.

the whole reaction, and only just before the end a slight deviation seems to occur. The nucleation and growth are mainly controlled by diffusion and a first-order process may influence the growth at the latest stages of the reaction. It must be kept in mind that the discussion of possible mechanisms based on the exponent *m* is not always straightforward. The values for *m* often deviate severely from the theoretical values listed in Table 2 and there are several reasons for these experimental findings. The simplest assumption is that reactions with different mechanisms proceed in parallel and/or in succession, yielding values different from theoretical ones.[44−46] We note that the values for *m* discussed above deviate from theoretical values, but they are in the range for diffusion-controlled mechanisms during the first stage of the reactions with stronger deviations from theoretical values for the later stage. The rate constant *k* and the half-life time exhibit a clear temperature dependence. While the half-life time decreases with increasing temperatures, the value for the rate constant increases (Table 2).

More detailed and rigorous analyses were performed comparing all models listed in Table 2 with the experimental data.[47−49] A plot of the experimental $t/t_{0.5}$ data ($t/t_{0.5}$ is the reaction time at $\alpha = 0.5$) vs α (Figure 6) allows a direct comparison with the different models under consideration. For $T > 110$ °C (Figure 6, $T = 115$ °C) the experimental data $\alpha < 0.7$ are in accordance with a diffusion control followed by a change toward the first-order mechanism F1 for $\alpha > 0.7$. When the time-dependent behavior of a reaction is scaled to 33%, a better discrimination between the models is possible for higher values of α. Hence, the plot of $t/t_{0.33}$ vs α (Figure 7, $T = 115$ °C) confirms the change of the mechanism at later stages of the reaction. For $T \leq 110$ °C the analysis of the data (Figure 8) suggests that diffusion (D2 and/or D3) is the rate-limiting process for the crystal growth, but a definite decision is not possible, in agreement with the results from the SH analysis (Figure 9). The deviations discussed above are also observed in the so-called Austin-Rickett plots[50] (Figure 10).

The activation energy E_A was determined with the Arrhenius equation using the *k* values of the first part of the reactions (Table 2). The plot ln *k* vs $1/T$ yields a straight line and $E_A = 42$ kJ/mol is obtained (Figure 11). This result is comparable with values found in the literature.[13,15]

At the end of the formation of $[Co(tren)][Sb_2S_4]$, reflections of a second crystalline phase appear in the spectra and several new reflections start to grow simultaneously (Figure 12). This phenomenon is independent from temperature and is observed at the latest stages of every reaction. The second phase was identified as $[tren]_x[Sb_{21}S_{34}]$. Unfortunately, the (102) reflection of $[Co(tren)][Sb_2S_4]$ and the (004/013) peak of the second phase coincide. Hence, the end of crystallization of $[Co(tren)][Sb_2S_4]$ was evaluated with the (002)

(44) Pradell, T.; Crespo, D.; Clavaguera, N.; Clavaguera-Mora, M. T. *J. Phys. Condens. Matter* **1998**, *10*, 3833.
(45) Fanfoni, M.; Tomellini, M. *Il Nuovo Cimento* **1998**, *20*, 1171.
(46) Castro, M.; Domínguez-Adame, F.; Sánchez, A.; Podríguez, T. *Appl. Phys. Lett.* **1999**, *75*, 2205.
(47) Avrami, M. *J. Chem. Phys.* **1939**, *7*, 1103.
(48) Avrami, M. *J. Chem. Phys.* **1940**, *8*, 212.
(49) Avrami, M. *J. Chem. Phys.* **1941**, *9*, 177.
(50) Austin, J. B.; Rickett, R. L. *Trans. AIME* **1939**, *135*, 396.

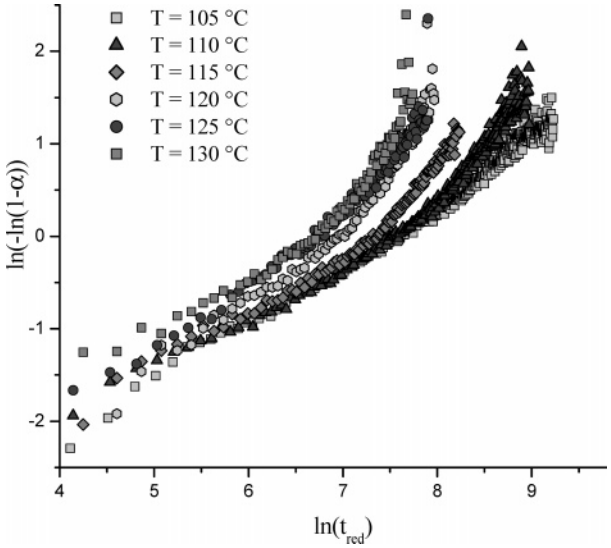

Figure 9. Sharp-Hanckock plots for all temperatures.

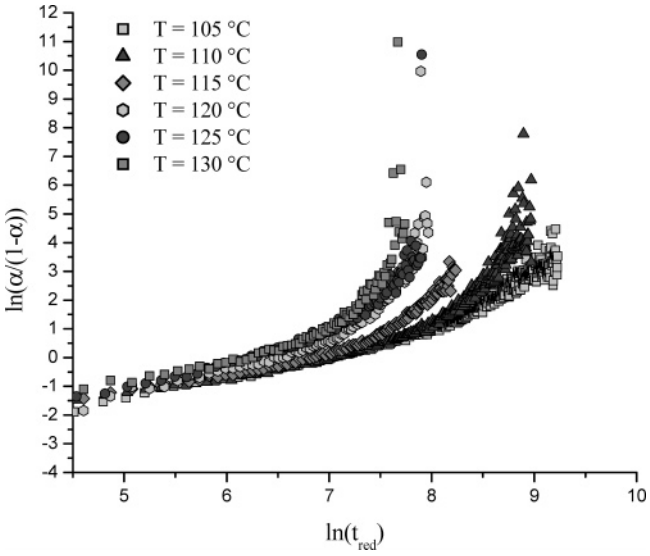

Figure 10. Austin-Rickett plots for all temperatures.

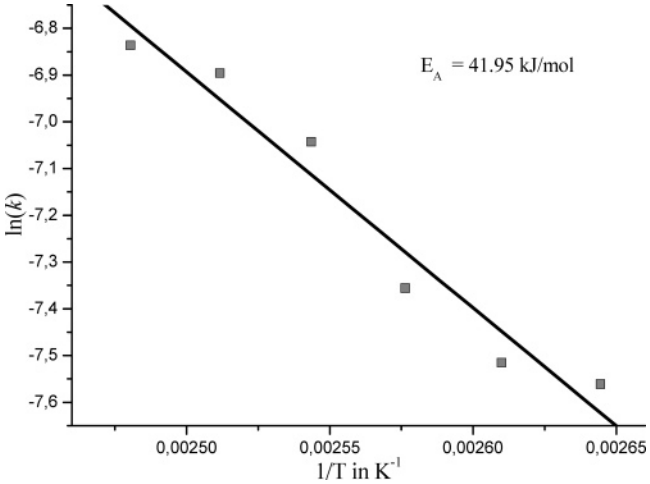

Figure 11. Arrhenius plot of ln k vs $1/T$ [K^{-1}] for the first stage of the reaction, determined from Sharp-Hancock plots.

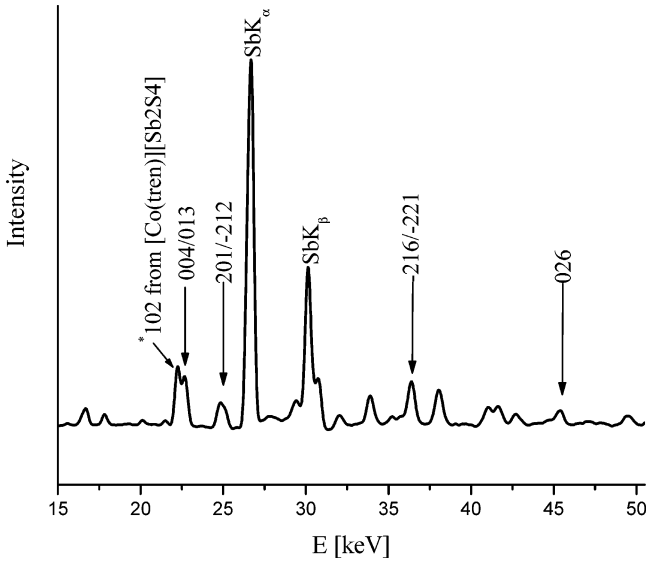

Figure 12. Energy dispersive diffraction patterns of [Co(tren)][Sb_2S_4] and the second phase. The indices of reflections of the second phase are indicated. Additionally the (102) reflection of [Co(tren)][Sb_2S_4] is marked.

reflection and for the second phase $[tren]_x[Sb_{21}S_{34}]$ the overlapping (202/−212) peak was used (Figure 12). The integrated intensity of the (002) peak of [Co(tren)][Sb_2S_4] passes a maximum which was then defined as the end of the formation of this phase. Exactly at this time the second phase starts to grow and the amount of the first compound starts to decrease (Figure 13).

An in situ experiment was performed for 14 h after the intensity of reflections of [Co(tren)][Sb_2S_4] just started to decrease to prove whether [Co(tren)][Sb_2S_4] is only a kind of intermediate. During the first 6 h the intensity of (002) of [Co(tren)][Sb_2S_4] drops and an equilibrium between the two phases is reached (Figure 13). This may be explained on the basis of a partial dissolution/amorphization of [Co(tren)][Sb_2S_4] and the simultaneous crystallization of the new phase. On a microscopic level the following may occur. At the point where the intensities of [Co(tren)][Sb_2S_4] start to decrease, the concentration of dissolved Co^{2+} cations is too low for further crystallization, and the transition metal free compound starts to crystallize. The formation of this new phase influences the equilibrium between solid [Co(tren)][Sb_2S_4] and the solution because the concentration of Sb^{3+}/S^{2-} is lowered due to crystallization of $[tren]_x[Sb_{21}S_{34}]$. The strong reduction of the concentration of Sb^{3+}/S^{2-} is accompanied by the partial dissolution of the Co-containing compound, yielding a new equilibrium for this complex system. To prove that [Co(tren)][Sb_2S_4] is not only dissolved by tren, the solid compound was filtered off after the reaction was complete and 2 mL of pure tren was added. No change in the spectra was observed within the next 4 h. The ratio between the two phases was constant, demonstrating that the pH value and the concentration of tren do not alter the equilibrium.

In about one-third of the in situ experiments highly interesting observations for reactions performed at $T \leq 120$ °C were made; i.e., a very different growth behavior of the reaction product was observed (Figure 14). After a temperature-dependent induction time only the (102) reflection starts to grow (Figure 14), and after another 28 min all other peaks of [Co(tren)][Sb_2S_4] occur and grow simultaneously. The position of the (102) reflection is slightly shifted to smaller energy values at the early stages of reaction (23.27 keV) and reaches 23.05 keV found in the other experiments

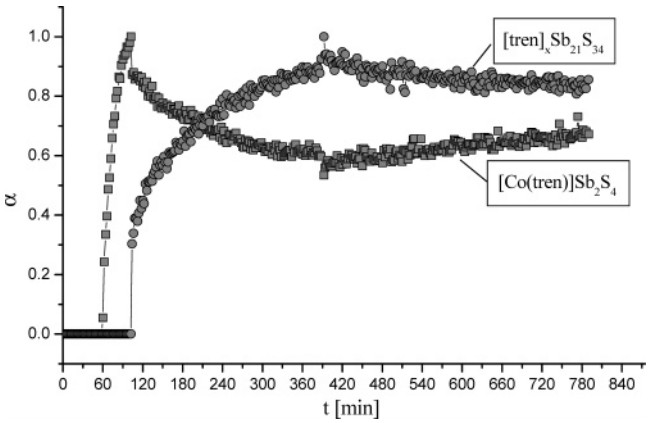

Figure 13. Extent of reaction α versus time for the (002) reflection of $[Co(tren)][Sb_2S_4]$ and the (202/−212) reflections of the second phase $[tren]_x[Sb_{21}S_{34}]$.

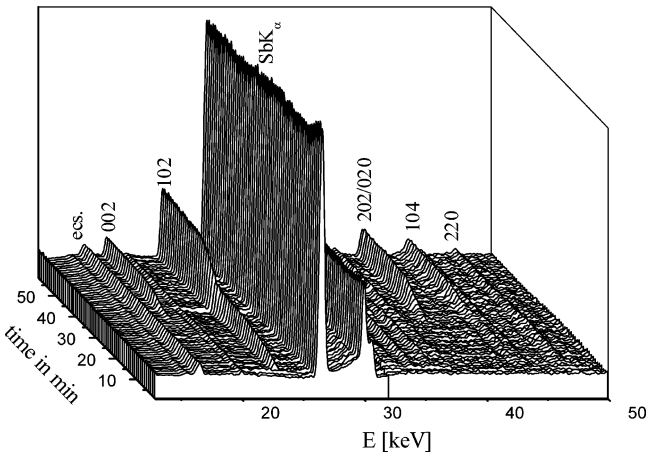

Figure 14. Time-resolved powder patterns recorded at 120 °C showing the different growth behavior. The indices of the most intense lines of the product phase and the Sb Kα fluorescence line are marked.

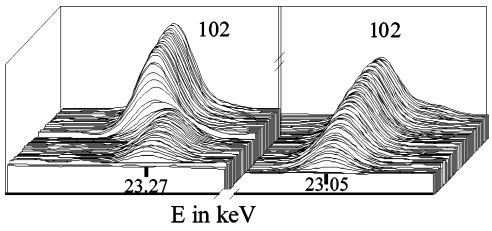

Figure 15. Comparison of the (102) reflection for the two different growth behaviors at 120 °C. Left: unusual growth behavior with peak shift; right: with normal growth mechanism.

discussed above (Figure 15). The most possible "parameter" responsible for this unusual observation is the ferromagnetic behavior of elemental Co. The slurry is stirred with a magnetic stirrer bar (see Experimental Section). When Co sticks at the surface of this bar, the dissolution of Co at $T \leq 120$ °C seems to have a random component. This effect is negligible for $T > 120$ °C due to faster dissolution of Co, yielding a concentration of Co^{2+} ions which is large enough for the nucleation and crystallization following the mechanisms presented above. We proved the hypothesis of this phenomenon and performed in situ experiments with $CoCl_2 \cdot 6H_2O$ as Co source. In all these experiments product growth proceeds following the reaction paths discussed in the previous section. This experimental finding supports our assumption that the velocity of dissolution of elemental cobalt has a significant influence on the reaction mechanism.

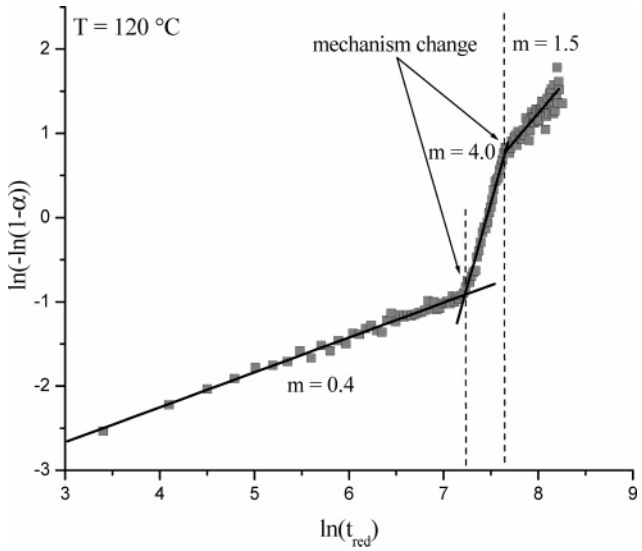

Figure 16. Sharp-Hanckock plot for the data at $T = 120$ °C for the product formed by the second reaction path.

The SH analysis of the data gives evidence that the crystallization kinetics occurs in three different steps, each being characterized by a different reaction exponent *m* (Figure 16). The values for *m* are about 0.4 ($\alpha < 0.33$) and 1.5 ($\alpha > 0.88$) for the first and third stage and deviate from the ideal values listed in Table 2. In the second part of the reaction where all peaks grow simultaneously the value for *m* of 4.0 is unusually large, but may be explained on the basis of constant nucleation.[51] An identical behavior was observed by O'Hare and co-workers[14] during the formation of the thiostannate TMA-SnS1 and was explained by strongly disordered layers which at later stages of reaction start to arrange, yielding the three-dimensional long-range order.

EXAFS Measurements. In the past decades many experiments were devoted to identify the soluble species of antimony sulfides in alkaline solutions. Different species were postulated, e.g., SbS_2^-, $Sb_2S_4^{2-}$, $Sb_4S_7^{2-}$,[52] SbS_3^{3-}, and SbS_4^{3-},[30,52,53] and $Sb_2S_6^{2-}$.[53] But until now it is not clear how Sb atoms are coordinated in basic sulfur-containing solutions. For a better understanding of the building mechanisms of thioantimonates it is important to identify primary building units existing in reaction solutions using EXAFS experiments.

Reference Measurements. Solutions with different concentrations of Sb/S in diethylentriamine were used as references (see Experimental Section). The edge jump scales linearly with the Sb concentration; i.e., lower Sb contents yield smaller jumps. The temperature effect onto the edge jump can be neglected. Interestingly, the spectra exhibit only different intensities of the peaks but no differences were observed for the shape of the XANES or EXAFS. This result shows that the coordination sphere of Sb is the same for all concentrations.

(51) Davies, A. T.; Sankar, G.; Catlow, C. R.; Clark, S. M. *J. Phys. Chem. B* **1997**, *101*, 10115.
(52) Wood, S. A. *Geochim. Cosmochim. Acta* **1989**, *53*, 237.
(53) Helz, G. R.; Valerio, M. S.; Capps, N. E. *Environ. Sci. Technol.* **2002**, *36*, 943.

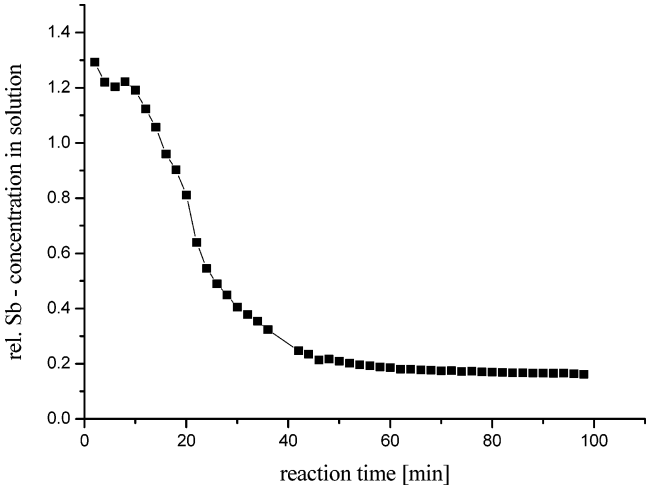

Figure 17. Evolution of the Sb K edge jump during the reaction.

Measurements during the Formation of [Co(tren)][Sb_2S_4]. The evolution of the Sb edge height during the reaction at 120 °C is shown in Figure 17. After a short induction time a maximum of the absorption jump $\Delta\mu x$ of 1.3 was reached and after 60 min the value decreased to 0.2. The change of the edge jump time proceeds not in a linear way but has a sigmoidal shape reminiscent of the curve for the extent of reaction presented in Figure 4. The two curves cannot be compared directly due to the different experimental conditions. The stirring was interrupted to collect the XAFS data (see Experimental Section); i.e., this interruption increases the reaction time. At the beginning of the reaction elemental Sb is dissolved and the Sb content in solution is very high. Within a few minutes the Sb content decreases dramatically, indicating that a solid product is formed which must be amorphous because it is not seen in EDXRD experiments. Hence, it can be assumed that long before crystallization of [Co(tren)][Sb_2S_4] an amorphous precursor is formed. The quality of EXAFS spectra of this amorphous solid was not good enough for an evaluation and the composition of the precursor is not known.

Evaluation of the Spectra. During the whole reaction only two different types of spectra were observed. At the beginning the spectra are similar to those recorded for reference A1 (see Experimental Section) and at the end the spectra are similar to those obtained with pellets of crystalline [Co(tren)][Sb_2S_4] (Figure 18). This observation suggests that [Co(tren)][Sb_2S_4] is either soluble or that small particles are present in the solution which do not sediment during the time after stirring was stopped. In another experiment the solution was not stirred for 2 h and care was taken that only the solution was investigated with EXAFS. Interestingly, the spectra were identical to those recorded at the beginning of the reaction, demonstrating that [Co(tren)][Sb_2S_4] is not dissolved and the spectra obtained at the end of the reaction were caused by small particles of [Co(tren)][Sb_2S_4].

Reactions with other Sb/S/amine slurries were also investigated (0.5 mmol of Sb, 1.5 mmol of S in 2 mL of 50% 2-aminoethylpiperazine at 160 °C; 0.5 mmol of Sb, 0.5 mmol of Mn, 1.2 mmol of S in 2 mL of 100% dien at 120 °C) to monitor the influence of the amine onto the formation of the SbS_x species. But for all solutions the spectra were similar; i.e., the environment of Sb in sulfur-containing amine solutions is identical. Temperature, volume, pH value, and the kind of amine have no measurable influence on the dissolved SbS_x species, which is a quite remarkable and surprising result.

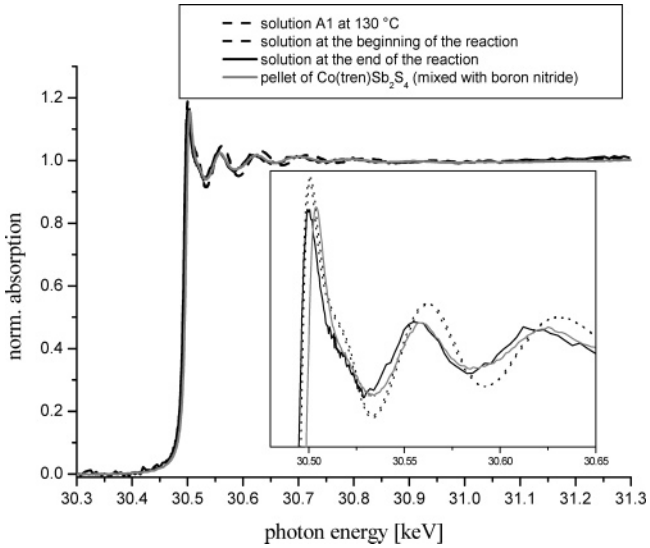

Figure 18. Changes of EXAFS spectra during the reaction.

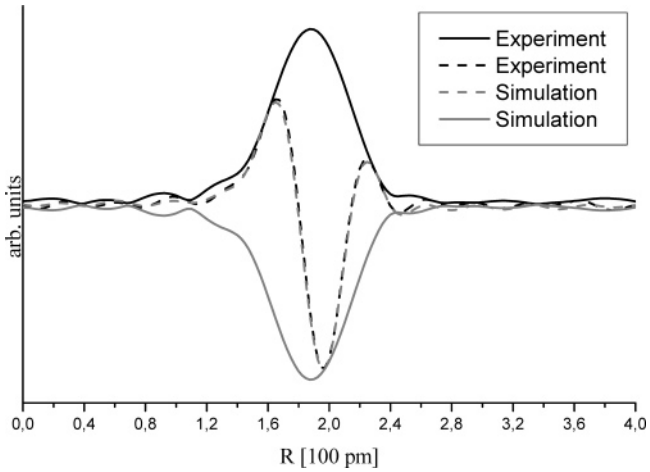

Figure 19. Experimental and simulated Fourier transformed $\chi(k)$. Theoretical phases and amplitudes calculated with SbS_3 and SbS_4 units.

Table 3. Results from EXAFS Simulations with Standard Deviations Given in Parentheses

	SbS_3	SbS_4	SbS_3	SbS_4
residual	3.51	3.59	1.60	3.58
coordination number	3 (fixed)	4 (fixed)	3.6 (free)	3.5 (free)
σ^2/Å^2	0.00189(3)	0.00386(4)	0.00308(2)	0.00295(3)

Simulations of EXAFS Spectra. The species in solution may be identified comparing simulated EXAFS spectra for different SbS_x species with the experimental data. In the literature[43−45] mainly three different structural species were suggested, i.e., a $Sb_2S_6^{6-}$ ring, the SbS_3^{3-} group, and a SbS_4^{3-} unit. The existence of the $Sb_2S_6^{6-}$ ring can be ruled out because the radial distance distribution (Figure 19) shows only one shell around Sb, but a $Sb_2S_6^{6-}$ ring requires a second shell, accounting for the Sb−Sb coordination. The two other models were simulated with Gaussian98 (see above) and protonated sulfur atoms had no influence on the geometry. The structurally optimized clusters were used for FEFF

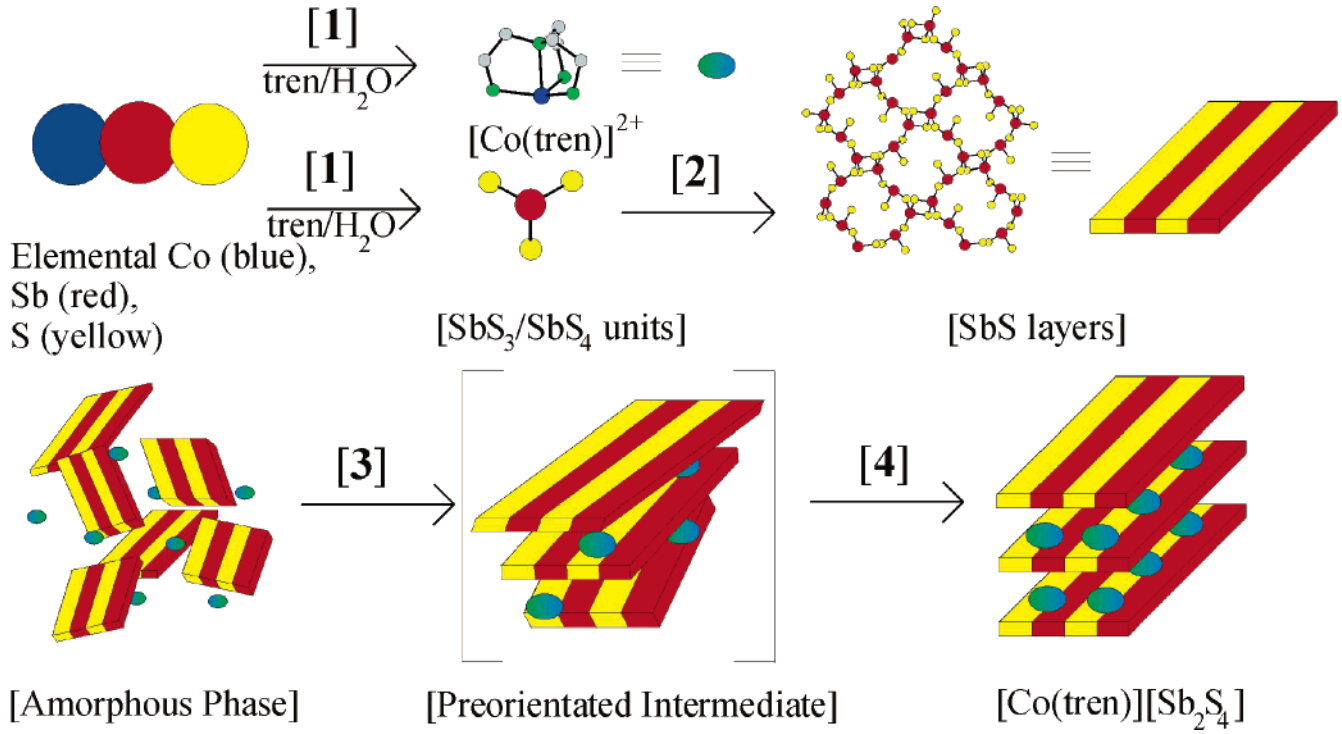

Figure 20. Reaction scheme for the formation of $[Co(tren)][Sb_2S_4]$.

calculations (see Experimental Section) and the results are summarized in Table 3.

The refinements performed with freely varying coordination numbers (CN) for either SbS_3 or SbS_4 always yield a value for CN near 3.5, suggesting that both species coexist in solution. Therefore, the spectrum was simulated containing a 1:1 mixture of SbS_3 and SbS_4 groups and the resulting FT($\chi(k)$) together with the theoretical XAFS function utilizing phases and amplitudes is shown in Figure 19. The calculated EXAFS function fits perfectly with the experimental $\chi(k)$ for both the phase and the amplitude. This result suggests that only these two groups are present in solution.

Conclusion

The synthesis of compounds under solvothermal conditions is in most cases a black box method; i.e., after a distinct reaction time the reaction vessels are removed from the furnaces and the products are then characterized. The products often consist of mixtures of different compounds and optimization of the synthesis is time-consuming because several reaction parameters have to be varied. In addition, crystalline precursors or intermediates may crystallize at short reaction times, which will never be "seen" using the conventional synthesis procedure. Such kinetically less stable compounds may have interesting physicochemical properties. In the present contribution we demonstrated that in situ EDXRD experiments are powerful for monitoring the evolution of the formation of a distinct compound so that phase-pure materials can be prepared. But for basic research the reaction mechanisms and kinetics occurring under solvothermal conditions are more interesting. A rigorous analysis of the results recorded as a function of different reaction parameters provides information about the kinetics and give hints about the reaction mechanisms. For the present system diffusion is the rate-limiting step, and at later stages the reaction exponents indicate more complex kinetics/mechanisms. When the synthesis of the title compound is performed with elemental Co at $T \leq 120$ °C, a random dissolution of Co influences the reaction path, which was immediately detected in the EDXRD spectra. At the beginning only the (102) reflection of the product starts to grow and slightly shifts with reaction time and at later stages of the reaction all other peaks of $[Co(tren)][Sb_2S_4]$ occur and grow simultaneously. These observations are reminiscent of a mechanism where first strong disordered layers are formed which then start to arrange during reaction progress, yielding the three-dimensional long-range ordered material.

The combination of in situ EDXRD with in situ EXAFS experiments provides information about the reaction starting from the very early stages until products start to crystallize. We have shown that the starting material is dissolved within a short period. According to the EXAFS analysis, only two different species are present in the solution. A drastic decrease of dissolved antimony species indicates that a solid product is formed which is not detected in the EDXRD spectra; i.e., the particle sizes are too small and/or the solid is amorphous.

Taking all results into account, possible reaction pathways can be postulated which is depicted in Figure 20. At the beginning of the reaction the starting material is very quickly dissolved (see Figure 20 path 1) and it can be assumed that Co is coordinated by the amine, yielding a $[Co(tren)]^{2+}$ complex. According to the EXAFS results, monomeric SbS_x units with $x = 3$ and 4 are formed. Further condensation (see path 2 in Figure 20) via common corners and/or edges leads to larger SbS aggregates, which precipitate and a solid amorphous phase is formed. For temperatures ≤ 120 °C a

preorientation (see path 3 in Figure 20) of the layers occurs and only the (102) reflection of the product starts to grow in the X-ray powder pattern. In contrast to this observation the normal reaction path does not proceed via this step and all product reflections grow simultaneously, which is sketched in Figure 20 as path 4.

Acknowledgment. The financial support of this work by the state of Schleswig-Holstein and the Deutsche Forschungsgemeinschaft (DFG) are acknowledged. We also thank Julia Wienold and Ulrich Ponkratz for their help at the beamlines X1 and F3 at HASYLAB.

CM051788T